Monthly Notices
of the
ROYAL ASTRONOMICAL SOCIETY

MNRAS **488,** 2989–3002 (2019)
Advance Access publication 2019 July 4

doi:10.1093/mnras/stz1748

Five new real-time detections of fast radio bursts with UTMOST

W. Farah [1]★ C. Flynn,[1,2] M. Bailes,[1,3] A. Jameson,[1,2] T. Bateman,[4] D. Campbell-Wilson,[4] C. K. Day,[1] A. T. Deller [1,2] A. J. Green,[4] V. Gupta,[1] R. Hunstead,[4] M. E. Lower [1,5] S. Osłowski [1] A. Parthasarathy [1] D. C. Price,[1,6] V. Ravi,[7,8] R. M. Shannon,[1,3] A. Sutherland,[4] D. Temby,[4] V. Venkatraman Krishnan [1,2,9] M. Caleb,[10,11] S.-W. Chang,[2,3,11] M. Cruces,[9] J. Roy,[12] V. Morello [10] C. A. Onken,[2,3,11] B. W. Stappers,[10] S. Webb[1,3] and C. Wolf [2,11]

[1]*Centre for Astrophysics and Supercomputing, Swinburne University of Technology, Mail H30, PO Box 218, Melbourne, VIC 3122, Australia*
[2]*ARC Centre of Excellence for All-sky Astrophysics (CAASTRO), Building A28, School of Physics, The University of Sydney, Sydney, NSW 2006, Australia*
[3]*ARC Centre of Excellence for Gravitational Wave Discovery (OzGrav), Swinburne University of Technology, Mail number H74, PO Box 218, Melbourne, VIC 3122, Australia*
[4]*Sydney Institute for Astronomy, School of Physics A28, University of Sydney, Sydney, NSW 2006, Australia*
[5]*CSIRO Astronomy and Space Science, Australia Telescope National Facility, Epping, NSW 1710, Australia*
[6]*Department of Astronomy, University of California Berkeley, 501 Campbell Hall, Berkeley, CA 94720, USA*
[7]*Center for Astrophysics | Harvard, Smithsonian, 60 Garden Street, Cambridge, MA 02138, USA*
[8]*Cahill Centre for Astronomy and Astrophysics, MC 249-17, California Institute of Technology, Pasadena, CA 91125, USA*
[9]*Max-Plank-Institute für Radioastronomie, Auf dem Hügel 69, D-53121 Bonn, Germany*
[10]*Jodrell Bank Centre for Astrophysics, School of Physics and Astronomy, The University of Manchester, Manchester M13 9PL, UK*
[11]*Research School of Astronomy and Astrophysics, Australian National University, Canberra, ACT 2611, Australia*
[12]*National Centre for Radio Astrophysics, Tata Institute of Fundamental Research, Pune 411 007, India*

Accepted 2019 June 17. Received 2019 June 16; in original form 2019 May 3

ABSTRACT

We detail a new fast radio burst (FRB) survey with the Molonglo Radio Telescope, in which six FRBs were detected between 2017 June and 2018 December. By using a real-time FRB detection system, we captured raw voltages for five of the six events, which allowed for coherent dedispersion and very high time resolution (10.24 μs) studies of the bursts. Five of the FRBs show temporal broadening consistent with interstellar and/or intergalactic scattering, with scattering time-scales ranging from 0.16 to 29.1 ms. One burst, FRB181017, shows remarkable temporal structure, with three peaks each separated by 1 ms. We searched for phase-coherence between the leading and trailing peaks and found none, ruling out lensing scenarios. Based on this survey, we calculate an all-sky rate at 843 MHz of 98^{+59}_{-39} events sky^{-1} d^{-1} to a fluence limit of 8 Jy ms: a factor of 7 below the rates estimated from the Parkes and ASKAP telescopes at 1.4 GHz assuming the ASKAP-derived spectral index $\alpha = -1.6$ ($F_\nu \propto \nu^\alpha$). Our results suggest that FRB spectra may turn over below 1 GHz. Optical, radio, and X-ray follow-up has been made for most of the reported bursts, with no associated transients found. No repeat bursts were found in the survey.

Key words: instrumentation: interferometers – methods: data analysis.

1 INTRODUCTION

Even though more than a decade has passed since they were first detected, fast radio bursts (FRBs) still defy explanation. Discovered by Lorimer et al. (2007), FRBs are millisecond-wide bursts seen in the radio part of the electromagnetic spectrum. The observed integrated electron column density, i.e. dispersion measure (DM), along the lines of sight of FRBs significantly exceeds that expected from the Milky Way, placing FRB sources at cosmological distances if the intergalactic medium (IGM) is the major contributor to the excess DM (Shannon et al. 2018).

Of the 69 FRBs published to date (FRBCAT;[1] Petroff et al. 2016), only two have been seen to repeat. The repeat bursts of FRB121102 allowed for an unambiguous localization of the FRB

★ E-mail: wfarah@swin.edu.au

[1]http://frbcat.org; visited 11/04/2019

source which resides in a star-forming region of a dwarf galaxy at redshift $z = 0.193$ (Bassa et al. 2017; Chatterjee et al. 2017; Marcote et al. 2017; Tendulkar et al. 2017). A large rotation measure (RM) of 10^5 rad m^{-2} reported by Michilli et al. (2018) places this FRB source in an extreme magneto-ionic environment. With the more recently discovered repeater FRB180814.J0422+73 by the CHIME radio telescope (CHIME/FRB Collaboration 2019b), repeating FRBs seem to share common characteristics, namely pulse-to-pulse variation with bursts showing complex temporal and spectral structure (Hessels et al. 2019). A few non-repeating FRBs show similar structure (e.g. Ravi et al. 2016; Farah et al. 2018a). This appears to be the only bridge connecting the potentially bifurcated classes, given that they occupy different regions of phase-space (Palaniswamy, Li & Zhang 2018), and that non-repeaters show modest RM (Caleb et al. 2018; Osłowski et al. 2019). Sub-pulse frequency drifts seen in the repeating FRBs are reminiscent of solar type III radio bursts, suggesting an analogous emission mechanism (CHIME/FRB Collaboration 2019b).

Scattering is characteristic of a pulsed radio signal traversing turbulent media, where the delayed time of arrival due to multipath propagation is manifested as an exponential tail in the signal pulse profile. It is not surprising that FRBs are underscattered with respect to Galactic pulsars with the same DM (Ravi 2019), given that the bulk of the FRB DM is likely to be due to propagation through the IGM (Shannon et al. 2018), which is thought to be less turbulent and hence less effective at scattering radio waves compared to the ISM (Koay & Macquart 2015). However, evidence supporting the existence of a scattering time-scale τ–DM relation for FRBs is accumulating (CHIME/FRB Collaboration 2019a; Ravi 2019), suggesting that scattering takes place in the IGM, possibly in the circumgalactic gas clumps of intervening galaxies (Vedantham & Phinney 2019). The scattered rays of radio emission of FRBs can also interfere with each other, giving rise to diffractive scintillation, evident as spectral modulation in the dynamic spectra of FRBs (e.g. Masui et al. 2015; Ravi et al. 2016; Farah et al. 2018a). Plasma lensing arising from scattering regions can enhance the radio flux of FRBs (Main et al. 2018) or even produce multiple images of the same burst with arrival times a few ms apart (Cordes et al. 2017).

Given their inferred cosmological distances, FRBs offer a means to probe the baryonic content of the IGM (Deng & Zhang 2014; Muñoz & Loeb 2018; Ravi et al. 2019) and galaxy haloes (McQuinn 2014). Moreover, FRBs can also probe the existence of massive compact halo objects if such objects are fortuitously aligned with FRB lines of sight (Zheng et al. 2014). The strong gravitational lensing of an FRB by a MACHO in the mass range of 20–100 $M_\odot$ would result in multiple images of the burst (Muñoz et al. 2016). Although the images would appear at an angular separation well below the resolving power of radio telescopes, the time of arrival of the pulses will differ by a few $\times(M_L/30\,M_\odot)$ ms, where M_L is the mass of the lens. Only if phase information is available, phase coherence can be searched for in temporarily resolved multipeaked FRBs in order to test lensing scenarios.

New generation telescopes are promising to revolutionize the FRB field in the very near future. ASKAP (Shannon et al. 2018) and CHIME (CHIME/FRB Collaboration 2019a) nearly doubled the total number of known FRBs only in the last year. The real-time FRB discovery system recently deployed on ASKAP will allow voltage capture that, in turn, can be used to image the sky, delivering a host galaxy association. The large ($\sim$250 deg^2) field of view of CHIME will allow the discovery of FRBs at a rate of a few per day (Connor et al. 2016). The Molonglo Observatory Synthesis Telescope (MOST) has been undergoing a transformation into an FRB-finding machine (Bailes et al. 2017). Caleb et al. (2017) reported the discovery of the first FRBs using this interferometer, placing the FRB source at least $>10^4$ km away from the telescope. More recently, Farah et al. (2018a) reported the blind detection of FRB170827 where the phase information of the detected radiation was preserved in the recorded data owing to its real-time discovery. Detailed analysis of the coherently dedispersed data of FRB170827 revealed rich spectral and temporal structure. UTMOST-2D is a project currently underway to fit the north–south (NS) arms of the Molonglo radio telescope with outriggers and a central detector to achieve arcsecond localization of FRBs (Day et al. in preparation). Other surveys dedicated to FRB searches are also currently in progress or in development (Wayth et al. 2011; van Leeuwen 2014; Stappers 2016; Bhattacharyya 2018; Keane et al. 2018; Law et al. 2018; Surnis et al. 2019). It is becoming standard to make use of machine learning algorithms to perform FRB candidate classification. Different approaches have been taken by different groups. For example, the FRB discovery pipelines described by Wagstaff et al. (2016) and Foster et al. (2018) are based on the traditional probabilistic machine learning algorithm random forest. Conversely, deep learning is also emerging as a promising technique for FRB discovery (Connor & van Leeuwen 2018; Zhang et al. 2018; Agarwal et al. 2019).

In this paper, we report the discovery of five new FRBs using the Molonglo radio telescope. We summarize the observing set-up and time-on-sky spent searching for FRBs in Section 2. In Section 3, we describe our machine learning based, real-time FRB detection pipeline. We detail our new discoveries in Section 4, and derive our FRB rates in Section 5. We describe the follow-up campaign in Section 6 and draw our conclusions in Section 7.

2 UTMOST AND FRB SEARCHES

MOST is located some 40 km east of Canberra, Australia. It is a Mills-Cross interferometer, comprised of two fully steerable east–west (EW) arms, each 778 m long with a total of 18 000 m^2 collecting area. The UTMOST project transformed the MOST into a commensal pulsar-timing/FRB-finding facility (Bailes et al. 2017; Jankowski et al. 2019), operating at 843 MHz, with a bandwidth of 31.25 MHz. Using this telescope, nine FRBs have been found to date. Three of these are reported in Caleb et al. (2017), and another is reported in detail in Farah et al. (2018a). In this paper, we describe the five additional events in detail and derive improved population properties of FRBs at 843 MHz.

Caleb et al. (2017) estimated a rate of 78^{+124}_{-57} events sky^{-1} d^{-1} at 843 MHz above a fluence of 11 Jy ms (a limit we revise to 15 Jy ms, see Section 5). These first three FRBs were found when the system had frequency channels 0.78 MHz-width so the effects of DM smearing were quite pronounced. The system has since been upgraded to 0.097 MHz-width channels, significantly improving our spectral resolution for the subsequent FRBs. The temporal resolution has been also improved from 655 to 327 μs, increasing our sensitivity to events narrow in time.

To search for FRBs, Molonglo's 4×2.8 deg^2 primary beam is tiled with consecutive, overlapping narrow strips. These 'fan-beams' are narrow in the EW direction [full width at half-maximum (FWHM) $\approx$ 45 arcsec], but broad in the north–south direction (FWHM $\approx 2.8^\circ$), meaning that host galaxy identification is not possible for detected FRBs. UTMOST-2D, a project currently under development, will make use of the NS arms of the telescope to achieve arcsecond localization of FRBs.

2.1 Live FRB discovery pipeline

The telescope operates in a band affected by interference caused by mobile phone handset transmissions. These sources of radio frequency interference (RFI) dominate false positives and were typically removed via human inspection of the data each morning. We describe here a fully automated system that performs this classification on the live data sufficiently rapidly to achieve voltage capture of the data for good candidates.

Voltage capture of interesting events is made in narrow time windows that encompass the dispersion smearing time, taking place after a real-time detection and classification before the observations are down-sampled and saved to disc. The time and frequency resolutions of UTMOST's final data product for human inspection after voltage capture are, respectively, 8 and 64 times higher than the data retained for usual offline analysis. The FRBs detected by Caleb et al. (2017) using the offline pipeline are sampled at 655 μs and 0.78 MHz; structure on smaller time and frequency intervals was completely unseen in the data.

Moreover, search-mode data suffer from interchannel and intrachannel DM-smearing. Algorithms usually reverse the effect of intrachannel dispersion by shifting each individual channel backwards in time – a process called incoherent dedispersion. On the other hand, coherent dedispersion makes use of the phase information preserved in raw data (complex voltages) of the receiver in order to completely correct for dispersion. However, the latter process is computationally expensive and is rarely used when searching blindly for FRBs in real-time.

2.2 Sensitivity improvements

The sensitivity of the EW arms was substantially improved in 2017 after converting the facility into a transit-only instrument only. Although the advantage of UTMOST's rotating ring antennas was achieving mechanical phasing in the EW direction, breakages and faults occurred on regular basis, and, thus, the EW slewing system was retired.

The 7744 ring antennas were aligned to the meridian over a four month period from early-to mid-2017. This was performed on a module-by-module basis, and regular observations of the bright pulsar Vela transiting the meridian were performed to validate the alignment and track the sensitivity increases. The result was a factor ≈2 increase on average in the system sensitivity, which was achieved by 2017 June. Since then, observations have been done entirely in transit mode, as the object of interest crossed the meridian.

2.3 Time on sky

Observations at MOST are performed almost completely autonomously using the dedicated Survey for Magnetars, Intermittent pulsars, RRATs and FRBs (SMIRF) scheduler. While the comprehensive description of the software is left to an upcoming paper (Venkatraman Krishnan et al. 2019), we briefly describe its mode of operation. SMIRF schedules which fields to observe, given local sidereal time and a pre-defined cadence list of FRB fields, pulsars, and pulsar search-pointings. A unique feature of UTMOST and SMIRF is that pulsar timing, periodicity and single-pulse pulsar searching, and FRB blind searching can be done commensally and in real-time. This automated scheduler achieved very substantial efficiency gains over its precursor, in addition to the increased sensitivity, such that we can now regularly time about 400 pulsars

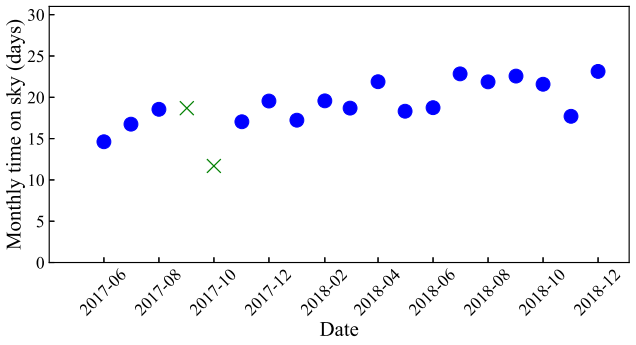

Figure 1. Number of days in each month of FRB-search time on sky over the course of the present survey. Blue circles show the monthly time-on-sky, while green crosses show two months where the time-on-sky had to be interpolated after a RAID failure led to the corruption of some metadata (search data were ordinarily processed prior to the failure). The efficiency of the system has been steadily increasing since the deployment of the SMIRF scheduler, along with the stability of the mechanical and electronic system.

on a weekly basis, do follow-up monitoring of known FRB fields and monitor the system sensitivity. Moreover, the SMIRF scheduler has the potential to observe phase calibrators if needed, although this feature has yet to be used; human intervention is still necessary to decide on the quality of a calibration and whether or not a phase solution should be applied. In general, the system is proving to be stable enough that phase calibration need only be performed every few days, unless the phase solution is lost (e.g. to power outages).

After the completion of the meridian drive and alignment of the EW feed antennas, 344 d on sky of FRB searching were completed between early 2017 June and 2018 December. Fig. 1 shows the monthly time on sky for the survey described above. A disc failure due to a power outage in 2017 October resulted in the corruption of meta-data for the months of 2017 September and October. We replaced the corresponding two data points in Fig. 1 for these months with the median of the monthly time on sky and median−7 d (to reflect the time lost on sky), respectively. Fig. 2 shows in Right Ascension and Declination (RA, Dec.) fields in which pulsars are timed or searched for commensally searching for FRBs in blue, fields in which we have done FRB follow-up in red, and finally grey shows fields where we solely search for FRBs, including 24 h scans of the sky at fixed declination. This strategy is employed if one of the telescope arms fails, and over the summer break when no staff are on site. Our off-sky time is due to scheduled monthly maintenance, telescope repairs, slew time, calibration and weather conditions.

3 FRB DETECTION PIPELINE

UTMOST's real-time FRB discovery system is based on the graphics processing unit (GPU) program HEIMDALL (Barsdell 2012). HEIMDALL performs dedispersion over a range of DM trials[2] (0–2000 pc cm^{-3}) and then performs a variable width boxcar convolution on the time-series to determine the optimal width of a candidate burst. Due to the harsh RFI environment on site, HEIMDALL produces candidates of the order of millions per day, with most being characterized as 5 MHz and a few millisecond-wide impulsive bursts. In order to deal with the large influx of

[2]Increased to 5000 since October 2018; see text.

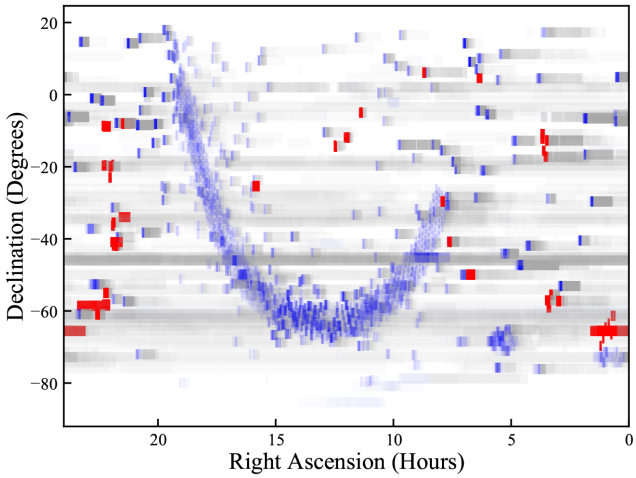

Figure 2. Regions of the sky surveyed by UTMOST in the time period between 2017 June and 2018 December. Grey represents observations of FRB-only fields, blue represents commensal pulsar observations/searches and FRB searches, and red regions mark FRB fields followed up by UTMOST. Colour depth indicates the integration times on sky.

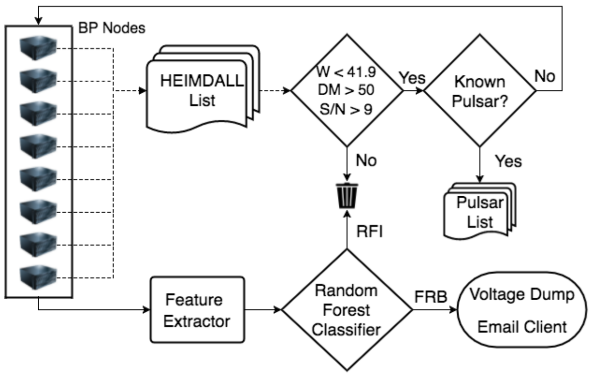

Figure 3. Schematic showing the signal path of the UTMOST detection pipeline. The processing time of any given candidate is typically ∼20 s. For widths ≥ 41.9 ms or DM $< 50\,\mathrm{pc\,cm^{-3}}$ the false positive rate due to RFI becomes unmanageable within the target processing time.

candidates, we have developed a low latency machine learning based candidate classification pipeline using the random forest algorithm (Breiman 2001). A random forest is a supervised machine learning algorithm that can be described as an aggregation of multiple decision trees that, collectively, form a robust classifier or regressor. The classification system is described in detail in the following sections.

In Fig. 3, we show a schematic describing the signal path. Beam-formed data (i.e. fan-beams) are analysed on the beam processing (BP) nodes by HEIMDALL, where they are held in RAM typically for 24 s [for a detailed description of the UTMOST processing backend, see Bailes et al. (2017)]. The HEIMDALL list of candidates is then checked against a known-pulsars list on a server. The list is then passed back to the respective BP node where feature extraction and candidate classification is performed. In order to successfully trigger a voltage capture, the runtime of the whole process should not exceed the length of the data on the RAM ring-buffers.

3.1 Training set

In general, a supervised machine learning algorithm undergoes a phase of 'training', where the algorithm is typically presented with a set of labelled data. The hyperparameters of the model are adjusted during the training phase such that the model is able to classify a similar but unfamiliar set as accurately as possible. A total of ∼10 000 candidates – comprised of single pulses from various pulsars, artefacts, and RFI-contaminated data – were collected in order to build a two-class training set used for the UTMOST real time classifier.

3.2 Pre-classifier candidate filtering

A first stage of filtering is applied on the candidates output, from HEIMDALL. All candidates with S/N <9, width ≥ 41.9 ms, or DM $< 50\mathrm{pc\,cm^{-3}}$ are rejected as probable artefacts. For widths ≥ 41.9 ms or DM $< 50\,\mathrm{pc\,cm^{-3}}$ the false-positive rate due to RFI becomes unmanageable. Each of the remaining candidates are then checked against a pulsar catalogue and is marked as a from pulsar if its DM lies within 50 per cent of the pulsar's DM and its position on sky is within ± 2 fan-beams of the pulsar's position (a pulse has a chance to be detected simultaneously in two neighbouring fan-beams, as the fan-beams are spaced an FWHM apart in normal observing). Single pulses from pulsars are still presented to the classifier and logged; however, observers are not notified about these events.

3.3 Feature extraction

The candidates that pass the pre-classifier filter are input to a feature extraction stage, where a list of predictors are extracted from the frequency−time data. These features are carefully engineered statistics that are capable of characterizing the noise and signal of a given candidate. The list of predictors presented to the classifier are the following:

(i) Modulation index, defined as

$$M = \frac{\sqrt{\langle I(\nu,t)^2\rangle_{\nu,t} - \langle I(\nu,t)\rangle^2_{\nu,t}}}{\langle I(\nu,t)\rangle_{\nu,t}}, \quad (1)$$

where $I(\nu, t)$ is the intensity in the event window[3] of the candidate. A time-averaged modulation index is also computed, described as the following:

$$\overline{M} = \frac{\sqrt{\langle \overline{I(\nu)}^2\rangle_{\nu} - \langle \overline{I(\nu)}\rangle^2_{\nu}}}{\langle \overline{I(\nu)}\rangle_{\nu}}, \quad (2)$$

where $\overline{I(\nu)} = \langle I(\nu,t)\rangle_t$ is the time-averaged spectrum of the FRB candidate.

(ii) The width of the candidate in data samples.

(iii) Fraction of power in each of the three RFI-dominated 5 MHz bands, centred at 842.5, 837.5, and 832.5 MHz:

$$Fp_i = \frac{\sum_{\nu_s^i}^{\nu_e^i}\sum_t I(\nu,t)}{\sum_\nu\sum_t I(\nu,t)}, \quad (3)$$

where ν_s^i and ν_e^i are the start and end frequencies of each of the RFI bands.

[3]The event window is defined as the dedispersed frequency–time matrix, where the DM and width of the event window are chosen to optimally maximize S/N.

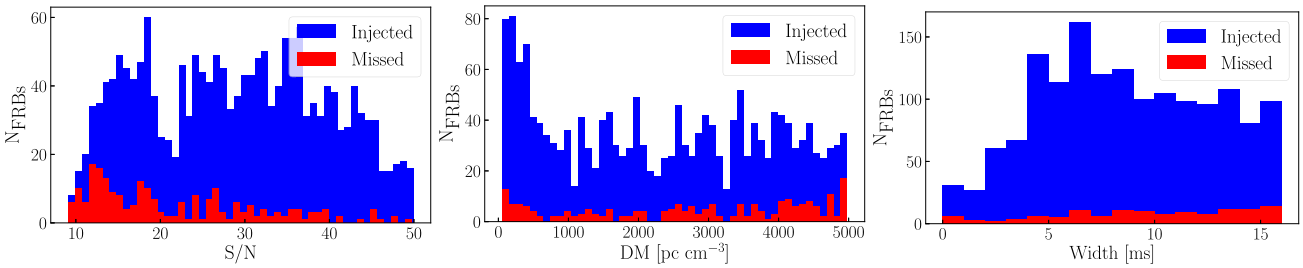

Figure 4. Distribution of S/N (left-hand panel), DM (middle panel), and width (right-hand panel) of the ∼2000 FRBs that were injected into UTMOST live stream data. In our live injection system, we aimed at keeping the distribution of mock FRBs uniform in width, S/N, and DM. However, simulating the effect of DM-smearing resulted in artificial broadening of most of the narrow FRBs. To ensure reasonable sampling in the narrow-width region, we injected a few additional low DM narrow FRBs. The distribution of FRBs missed by our pipelines are plotted in red.

(iv) The statistics and the *p*-values of the Kolmogorov–Smirnov and Shapiro–Wilk tests, comparing the time-averaged spectrum to a normal distribution.

(v) The mean (μ) and standard deviation (σ) of the event window.

(vi) The mean and standard deviation of windows with the same widths before and after the event window.

(vii) The ratio of number of pixels with intensity values greater than the mean, the mean plus one, and plus two times the standard deviation of the event window, to the total number of pixels in the event window, i.e.,

$$f_i = \frac{N(I(\nu, t) > \mu + i\sigma)}{N(I(\nu, t))}, \tag{4}$$

where $i = 0$, 1, 2 and $N(I(\nu, t))$ is the total number of pixels in a given event window.

3.4 Validation

When the model was first deployed on the live system of UTMOST, the pulsar catalogue used for candidate cross-checking only consisted of pulsars that were already present in the training set. Single pulses from pulsars not listed in that catalogue are treated as candidates and are presented to the classifier for evaluation. Observers would then receive email notifications of 'new' detected pulsars, and, upon a user's validation, the catalogue is appended with the pulsar names. More than 130 pulsars have been blindly 'discovered' by the pipeline. Over 250 000 pulses (excluding those from the bright pulsars Vela and J1644–4559) have been detected during the survey.

In order to better understand the detection completeness of our system, we have developed a live injection system of simulated FRBs. A set of mock FRBs with a known set of S/N, DM, width, and scattering properties are held in a database on disc. The current mock injection algorithm operates in total power (detected data) space, and injections are performed directly on live data streams of individual fan-beams. In Fig. 4, we show the distribution of S/N, DM and width for the ∼2000 injected FRBs (blue) and FRBs missed by our pipelines (red). The fake FRB parameter space was sampled uniformly in the S/N range of [9,50], DM of [50,5000] pc cm^{-3}, and width of [0,16] ms. Due to computational constraints, we did not sample the region with width <16 ms as thoroughly as width >16 ms. However, we do expect that the efficiency of our pipelines to decrease with increasing pulse widths. In general, we do not see any obvious trends in the missing fraction of fake FRBs, and work is in progress to reduce the false negative rate of our pipelines. Ninety per cent of the ∼2000 injected FRBs were blindly recovered, establishing our confidence in the overall detection and classification pipelines. Plans are currently set to extend the algorithm to be able to inject FRBs in the complex-sampled data output of individual UTMOST modules. The main advantages are that mock FRBs injected at the voltage level have to pass through more of UTMOST's processing pipeline, such as the delay engine, RFI mitigation subroutine, and the beamformer.

4 FRB DISCOVERIES

Over 344 d of on-sky observations, the survey yielded six FRBs that passed our automatic and visual verification tests (Table 1). One of these, FRB170827 has already been reported by Farah et al. (2018a). Here, we report the discovery of FRB170922, FRB180525, FRB181016, FRB181017, and FRB181228. All but one of these (FRB170922) were discovered in real-time, where a voltage capture was triggered, allowing for improved localization in the EW direction and coherent dedispersion (see Farah et al. 2018a). As part of our policy to publicize confirmed events, Astronomer's Telegrams were issued for all the above FRBs (Farah et al. 2017, 2018b,c,d). The dynamic spectra of the FRBs, and their frequency-averaged pulse profile are displayed in Figs 5 and 6.

The localization arc of the FRBs can be described as a second-order polynomial of the form

$$\mathrm{RA} = \mathrm{RA}_0 + a(\mathrm{Dec.} - \mathrm{Dec.}_0) + b(\mathrm{Dec.} - \mathrm{Dec.}_0)^2, \tag{5}$$

where RA_0 and $\mathrm{Dec.}_0$ are the coordinates of the most probable location. Parameters a and b are determined using a second-order polynomial least squares fit to the sky trace of the tied-array beam in which the S/N is maximized. We list the times of arrival, coordinates, and the corresponding localization arc parameters, and properties of our FRB sample in Table 1. The reported detection S/N represents the signal-to-noise ratio evaluated by the discovery algorithm, a value which is particularly valuable for source-count studies (see e.g. James et al. 2019). To compute flux densities, we use the radiometer equation:

$$S_{\mathrm{peak}} = \eta \times \mathrm{S/N} \times \frac{T_{\mathrm{sys}}}{G\sqrt{\mathrm{BW} \times W_{\mathrm{eq}}}}, \tag{6}$$

where η is the beam attenuation correction factor in the EW direction, $T_{\mathrm{sys}} = 330$ K is the system temperature, and G is the gain of the instrument, determined using the latest phase calibrator prior to each FRB detection, typically ∼1.7 K Jy^{-1}. BW = 31.25 MHz is the bandwidth of the Molonglo radio telescope, and W_{eq} is the equivalent width of the bursts. The equivalent width of an FRB represents the width of a top hat with height and area equal to the amplitude and area of the burst pulse profile. Due

Table 1. Arrival times, coordinates, and the properties of the FRBs reported in this paper. The coordinates (RA, Dec.) and (*Gl, Gb*) represent the centre of the localization arc described in equation (5).

	FRB179022	FRB180528	FRB181016	FRB181017	FRB181228
			Arrival time and coordinates		
Event time at 850 MHz UTC	2017-09-22 11:23:33.4	2018-05-28 04:24:00.9	2018-10-16 04:16:56.3	2018-10-17 10:24:37.4	2018-12-28 13:48:50.1
RA, Dec. (J2000)	21:29:51.22, −07:59:40.48	06:38:49.80, −49:53:59.0	15:46:20.84, −25:24:32.6	22:05:54.82, −08:50:34.22	06:09:23.64, −45:58:02.4
Gl, Gb	45.0683°, −38.7006°	258.8723°, −22.3530°	345.5101°, +22.6607°	50.0564°, +46.8816°	253.3519°, −26.1469°
RA_0 (h)	21.497561	6.647 167	15.772 456	22.098561	6.156567
$Dec._0$ (deg)	−7.994578	−49.899 722	−25.409 056	−8.842839	−45.967333
a^*	$3.808\,988 \times 10^{-5}$	$1.398\,369 \times 10^{-3}$	$9.641\,957 \times 10^{-4}$	$1.162\,544 \times 10^{-4}$	$1.057\,078 \times 10^{-3}$
b^*	$1.056\,944 \times 10^{-5}$	$-3.903\,834 \times 10^{-5}$	$-2.033\,868 \times 10^{-5}$	$4.269\,530 \times 10^{-6}$	$-2.784\,623 \times 10^{-5}$
Dec. range	[−12, −4]	[−54, −46]	[−30, −21]	[−13, −5]	[−50, −42]
			Measured properties		
HEIMDALL detection S/N	20	11	17	66	12
Dispersion measure, DM (pc cm^{-3})	1111 ± 1	899.3 ± 0.6	1982.8 ± 2.8	239.97 ± 0.03	354.2 ± 0.9
Scattering time at 835 MHz (ms)	$29.1^{+2.8}_{-2.6}$	$1.0^{+0.3}_{-0.4}$	$5.7^{+0.8}_{-0.8}$	$158^{+8}_{-7} \times 10^{-3}$	<0.2
Gaussian width (ms)	$1.8^{+0.4}_{-0.4}$	$0.5^{+0.2}_{-0.1}$	$1.2^{+0.3}_{-0.3}$	$(73^{+4}_{-4}, 82^{+16}_{-15}, 87^{+7}_{-9}) \times 10^{-3}$	$0.25^{+0.09}_{-0.06}, 0.7^{+0.3}_{-0.4}$
Equivalent width (ms)	$34.1^{+2.6}_{-2.8}$	$2.0^{+0.2}_{-0.2}$	$8.6^{+0.7}_{-0.8}$	0.32, 0.33, 0.35	$1.24^{+0.13}_{-0.15}$
Peak separation (ms)	–	–	–	$1.14 \pm 0.01, 0.75 \pm 0.01$	1.1 ± 0.2
Observed peak flux density, S_{peak} (Jy)	5.19	15.75	10.19	161, 39, 89	19.23
Fluence† (Jy ms)	>177	>32	>87	>52, 13, 31	>24
			Model-dependent properties		
$DM^{\ddagger}_{MW}$ (pc cm^{-3})	45	70	89	39	58
$\tau^{\ddagger}_{MW}$ (μs) (at 835 MHz)	0.31	0.76	1.58	0.21	0.49
Max. inferred z	1.2	0.9	2.2	0.2	0.3
Max. comoving distance (Gpc)	3.8	3.1	5.5	0.8	1.2
Max. luminosity distance (Gpc)	8.1	5.9	17.4	0.9	1.6
Max. isotropic energy (10^{40} erg)	21.2	2.4	31.9	0.4	0.2
Peak luminosity (10^{43} erg s^{-1})	1.3	2.2	11.8	1.6	0.2

Notes. *See equation (5).
†Corrected for the known position of the FRB within the primary beam pattern in the east–west direction, but uncorrected for the (unknown) FRB position in the north–south direction.
‡According to NE2001 model.

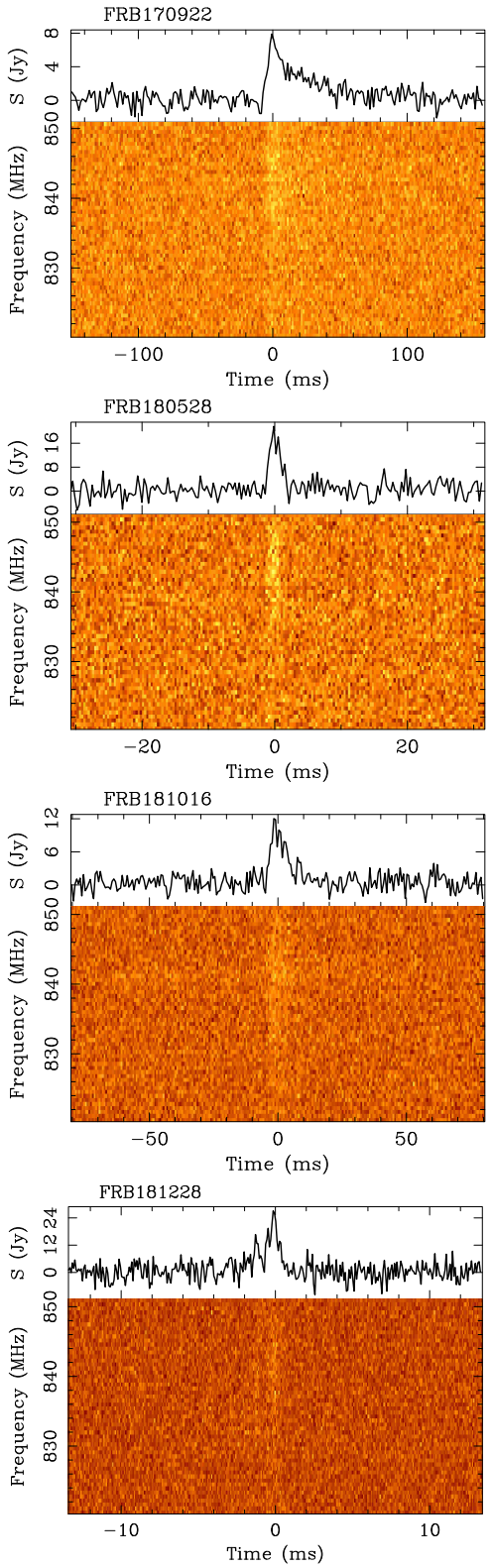

Figure 5. FRB170922, FRB180528, FRB181016, and FRB181228. In the lower panels of each plot, we show the dynamic spectrum, and in the upper panels, the flux density S in Jy versus time. Note that UTMOST's resonant cavity is more sensitive in the range 835–850 than 820–835 MHz. FRB170922 shows the largest scattering tail measured for an FRB with $\tau_d = 29.1^{+2.8}_{-2.6}$ ms.

to the unconstrained position of the bursts in the NS direction, the measured flux densities represent lower limits of the values assuming the bursts were observed close to the beam centre.

We follow Zhang (2018) to compute the maximum DM-inferred redshift of FRBs, assuming that the contribution of the host galaxies of FRBs to their measured DM is $\mathrm{DM_{host}} = 50\,\mathrm{pc\,cm^{-3}}$. We follow Hogg (1999) to estimate the in-band isotropic energy of FRBs:

$$E = \frac{4\pi D_{\mathrm{L}}^2}{(1+z)^{1+\alpha}} F_{\nu_c} \mathrm{BW}, \tag{7}$$

where F_{ν_c} is the fluence of the FRB, BW is the bandwidth of the observing instrument, D_{L} is the luminosity distance, and α is the spectral index ($F \propto \nu^{\alpha}$). We adopt the following cosmology (Planck Collaboration 2016): $H_0 = 67.74\,\mathrm{km\,s^{-1}\,Mpc^{-1}}$ as the Hubble parameter, $\Omega_{\mathrm{b}} = 0.0486$, $\Omega_{\mathrm{m}} = 0.3089$, and $\Omega_{\Lambda} = 0.6911$ as the baryonic matter, total matter, and dark energy density parameters, respectively, and we make use of the cosmology calculator CosmoCalc (Wright 2006).

A radio signal traversing turbulent media undergoes multipath propagation, resulting in delayed times of arrival due to the additional light travel distance. This effect is evident as a trailing exponential tail on a dedispersed pulse profile. Pulse broadening is modelled as a Gaussian convolved with a one sided exponential of the form

$$\mathscr{M} = A \times \exp\left[\frac{-(t-t_0)^2}{2\sigma^2}\right] * \left\{\exp\left[-\frac{t-t_0}{\tau_{\mathrm{d}}}\right] H(t-t_0)\right\}, \tag{8}$$

where $*$ denotes convolution. τ_{d} is the scattering time-scale, σ is the Gaussian width, and $H(t-t_0)$ is the Heaviside step function. Parameter estimation was performed using the BILBY package (Ashton et al. 2019), making use of the `pyMultiNest` sampler (Buchner et al. 2014). We used a Gaussian likelihood function for our parameter estimation, along with uniform priors on all the fitted parameters. The scattering time-scale measurements as a function of extragalactic DM of our latest FRBs are plotted in red in Fig. 7. A major current advantage of UTMOST is the capacity to capture voltages for FRBs, permitting scattering tails to be resolved and measured for narrower events than the bulk of FRBs to date at other facilities. Highly scattered low-DM FRBs are detectable in principle in all FRB surveys plotted in Fig. 7 but, to-date, have not been. When voltage capture becomes routine at other facilities, narrow but high DM events can be expected.

We show the observed and fitted profiles in Fig. 8, the posterior distributions of the Gaussian widths and the scattering time-scales are shown in Fig. 9. We note that all the FRBs presented here are overscattered with respect to the expectation from the Milky Way along their lines of sight, according to the NE2001 model (Cordes & Lazio 2002).

4.1 FRB170922

FRB170922 has a measured DM of 1111 $\mathrm{pc\,cm^{-3}}$ and shows a relatively large scattering tail, as can be seen in Fig. 5. We fit the profile using the above method and measure a scattering time-scale of $29.1^{+2.8}_{-2.6}$ ms, one of the largest for an FRB. FRB170922 was successfully discovered by UTMOST's live detection algorithm during a period of downtime, in which the system was recovering from a previous (false) trigger, which had taken place ∼20 s prior. The width of the FRB pulse is much larger than the inter-channel smearing time due to DM, and hence coherent dedispersion would have yielded no significant enhancement in S/N.

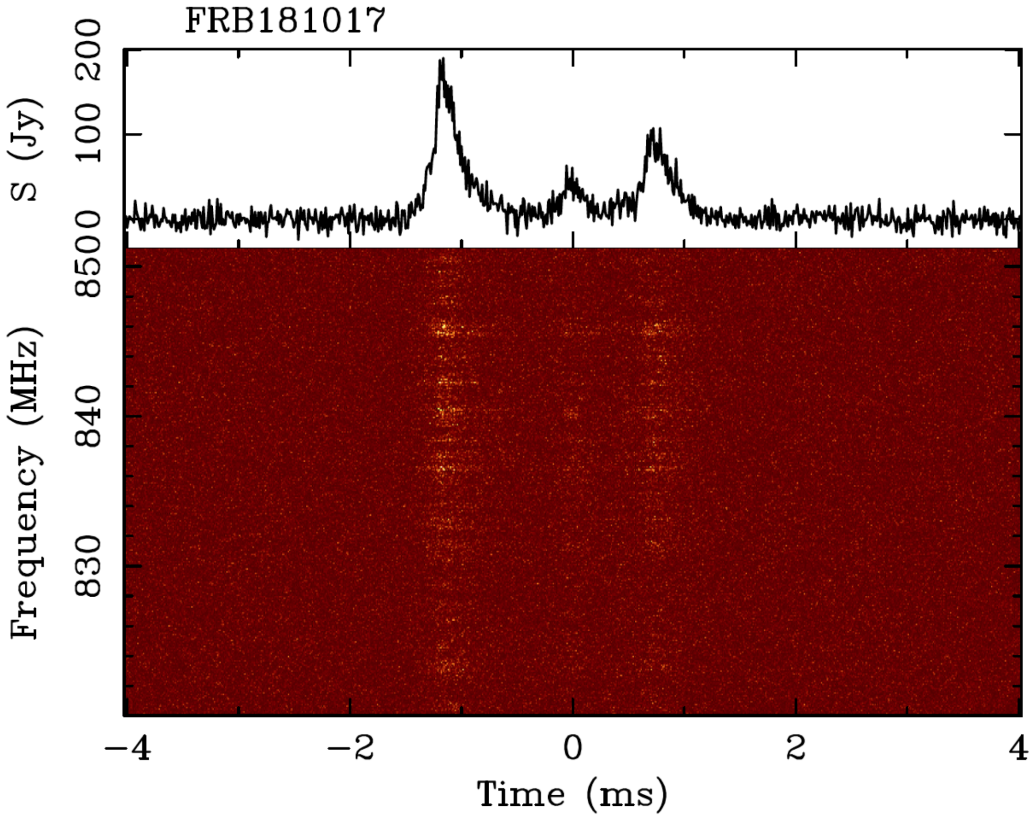

Figure 6. FRB181017: the triple-peaked FRB. The waterfall plot for the FRB is shown for frequency as a function of time. Voltage capture of the event yields much higher time resolution (10 μs) than we obtain from the off-line pipeline (655.36 μs). The frequency resolution is 97.66 kHz. The event shows a remarkable three peaked structure, with a spectrum which is quite similar across the peaks, similarly to what is seen in FRB170827. The three peaks have consistent scattering time-scales and pulse widths. This scattering time-scale would be associated with frequency structures at the kHz scale, far below the instrumental resolution. The striations in frequency are on scales of a few 100 kHz, and could be associated with the ISM (the NE2001 model predicts scintillation bandwidths at the position of the FRB of ≈2 MHz), although we cannot rule out they arise at the source or propagating through the host galaxy ISM and/or the IGM.

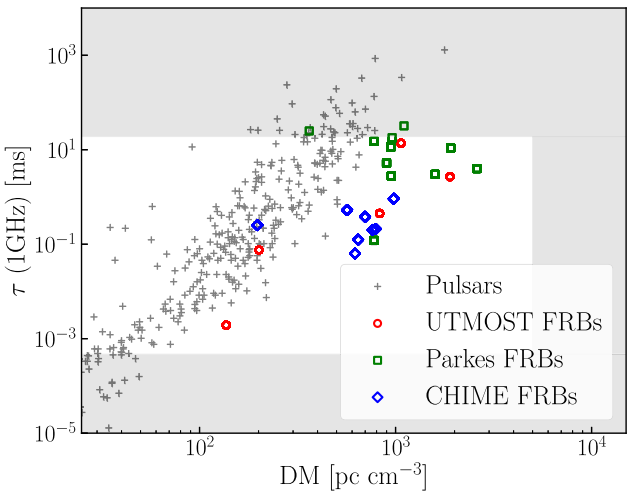

Figure 7. Broadening time-scale as a function of the extragalactic DM for FRBs, and versus DM for Galactic pulsars. Only those FRBs are shown for which the scattering time can be measured; upper limits are not shown. The general trend is for FRBs to show less scattering than pulsars at the same DM. Note that the grey regions indicate approximately where we would expect to be strongly biased against finding FRBs: (1) because the DM limit is 5000 pc cm^{-3} on the UTMOST survey, with similar lower limits pertaining at the other two surveys, and (2) because of the time resolution limits (10 μs and ≈40 ms for UTMOST).

4.2 FRB180528

The coherently dedispersed pulse profile of FRB180528 at its DM of 899 pc cm^{-3} shows hints of temporal broadening at high time resolution. Fitting the profile with the model defined in equation (8), we find that the scattering time-scale at 835 MHz is $\tau_{\rm d} = 0.95^{+0.33}_{-0.35}$ ms, a value consistent with 0 at the 3σ level. This is evident in Fig. 9 as the posterior distribution of $\tau_{\rm d}$ is unbounded at the lower edge of the prior range ($\tau_{\rm d} = 0$).

4.3 FRB181016

FRB181016 represents the highest DM FRB that UTMOST has discovered to date, with a DM of 1984 pc cm^{-3}. The burst detection caused us to increase the DM threshold limit of the live pipeline from 2000 to 5000 pc cm^{-3}. Given the observed fluence and the relatively high DM, FRB181016 is inferred to be one of the most luminous FRBs, with an average inferred isotropic luminosity of $L \sim 10^{44}$ erg s^{-1}. We measure a scattering time-scale of 5.7 ± 0.8 ms.

4.4 FRB181017

The dynamic spectrum of FRB181017 (Fig. 6) reveals rich spectral and temporal structure. Unresolved in the detection filter bank due to the low time resolution, the high time resolution time-series of FRB181017 shows three burst peaks separated in time by 1.14 ± 0.01 and 0.75 ± 0.01 ms.

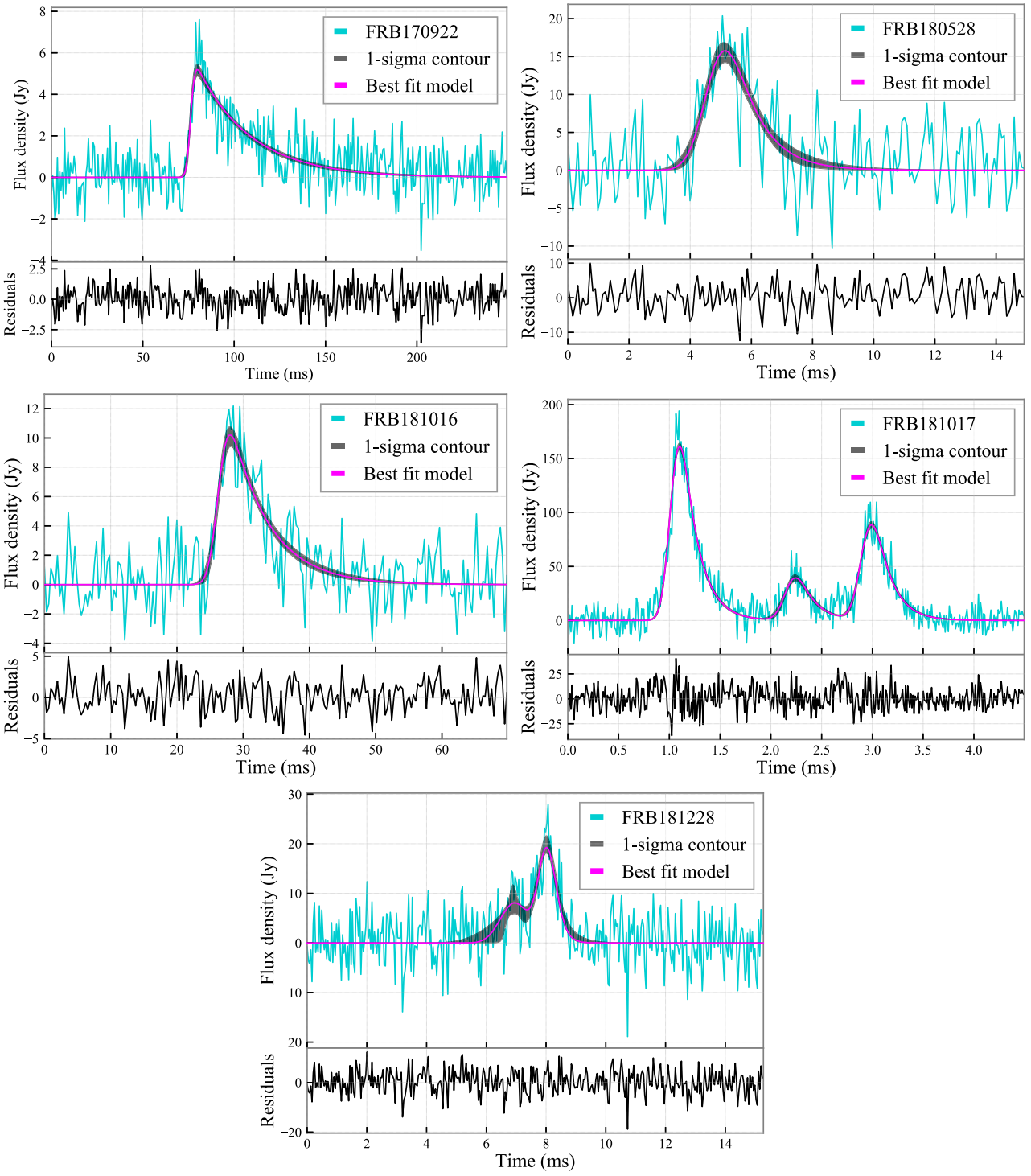

Figure 8. Frequency-averaged time-series of the five FRBs presented in this paper. The time-series of FRB170922, FRB180528, and FRB181016 are fitted with the model described in equation (8), whereas FRB181017 and FRB181228 are fitted with a modified model (see Sections 4.4 and 4.5).

As the three peaks show hints of scattering, we fit the pulse profile by a model consisting of a summation of three Gaussian distribution functions with variable widths, convolved with the same exponential scattering time-scale. We find that the (Gaussian) widths of the peaks are comparable, with a mean $= 80\,\mu s$, and the measured scattering time-scale is $\tau_d = 160\,\mu s$. We also fit the profile with a variable τ for each peak and find that the scattering is consistent between them. We measure the decorrelation bandwidth by fitting the constructed spectral autocorrelation function with a Gaussian function as described in Farah et al. (2018a). We find that the decorrelation bandwidth is $\nu_d = 0.36\,MHz$.

Given the resemblance in the temporal structure of the three features of the burst, we explore the hypothesis that the lagging peaks are copies of the leading one (e.g. Muñoz et al. 2016; Cordes

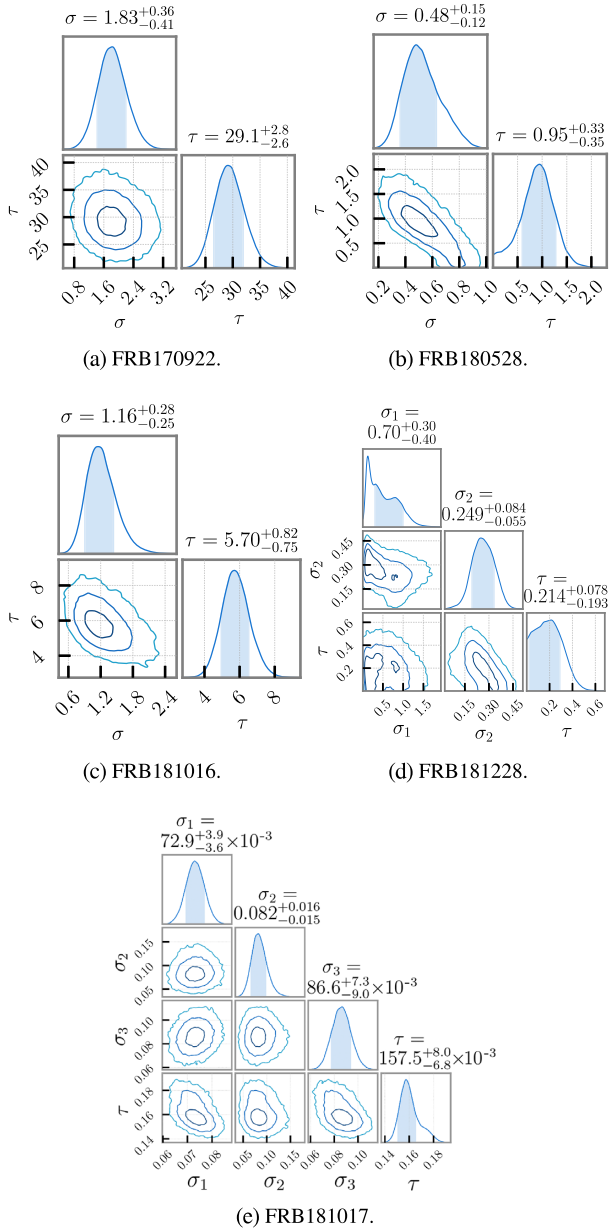

(a) FRB170922. (b) FRB180528. (c) FRB181016. (d) FRB181228. (e) FRB181017.

Figure 9. The posterior distributions of the Gaussian width (σ) and scattering time-scale (τ_d) for the fitted model (equation 8) for the new FRBs reported. All values shown are in ms.

et al. 2017) by searching for correlation in voltages between them. From the saved raw voltages, we first create a complex-sampled filter bank at the native time and frequency resolution of the instrument by placing a tied array beam on the best known position of the FRB. The filter bank is then coherently dedispersed using a custom-built dispersion-removal software.[4] A delayed signal traversing a different path might not encounter the same electron density as the main pulse, and hence might be dispersed differently. A small difference in DM between the pulses might de-cohere the cross-correlation product. For example, if one pulse is dispersed 0.1 pc cm^{-3} more than the other, the expected delay in arrival times between them, at the bottom of the UTMOST band, is ∼40 μs (or ∼4 time samples). Hence, we perform a grid search over DM by coherently dedispersing one of the pulses ±2 pc cm^{-3} with respect to the other, in steps of 0.01 pc cm^{-3} prior to cross-correlation.

For each frequency channel, we compute the cross-correlation of the dedispersed voltage stream $e(\nu, t, \mathrm{dm})$ with a delayed copy of itself that has been trial dedispersed, $e(\nu, t + \delta t, \mathrm{dm} + \delta\mathrm{dm})$:

$$\mathrm{V}(\nu, \delta\mathrm{t}) = \langle \mathrm{e}(\nu, \mathrm{t}, \mathrm{dm})\mathrm{e}^*(\nu, \mathrm{t} + \delta\mathrm{t}, \mathrm{dm} + \delta\mathrm{dm})\rangle, \quad (9)$$

where * represents the complex conjugate operator, and angular brackets denote time averaging. We select a windowing function that is approximately equal to the width of a single peak, and we search in the range $-500 < \delta t < 500$ time samples. For every sample delay δt, we calculate the *degree of coherence*,

$$\gamma(\delta t) = \frac{\widetilde{\mathrm{V}}(t, \delta t)}{\langle e(\nu, t)e^*(\nu, t)\rangle} = \frac{\widetilde{\mathrm{V}}(t, \delta t)}{|e(\nu, t)|^2}, \quad (10)$$

where $\widetilde{\mathrm{V}}(t, \delta t)$ is the lag spectrum computed by taking the inverse Fourier transform of $\mathrm{V}(\nu, \delta\mathrm{t})$, and the denominator represents the amplitude of the autocorrelation function. In the limiting cases, the two temporal peaks of FRB181017 at any given δt would be completely coherent (incoherent) if $|\gamma(\delta t)| = 1(0)$. We found no evidence that the temporal features of FRB181017 are phase correlated by placing a 5σ upper limit of 2.5 per cent on the degree of coherence between the three FRB peaks. We conclude that this triple-peaked structure is most likely intrinsic to the source emission.

4.5 FRB181228

A hint of a precursor is visible in the dynamic spectrum and the dedispersed time-series of FRB181228 as seen in Fig. 5. Similar to FRB181017, the pulse profile of FRB181228 was modelled using two Gaussians convolved with an exponential. The modelling of the pulse profile of this FRB proved challenging due to its low S/N evidenced by a large 1σ contour in the fit (Fig. 8) and its unbounded posteriors (Fig. 9). As the measured τ is consistent with being zero at the 2σ level ($\tau = 0.21^{+0.08}_{-0.19}$ ms), we consider this measurement as an upper limit.

5 FRB RATE AT 843 MHz

The present survey ran from 2017 June 1 to 2018 December 31 commensally with the UTMOST pulsar timing/searching program (SMIRF – Venkatraman Krishnan et al. 2019). We estimate the total amount of time spent by UTMOST on sky during the survey as 344 d. The survey yielded a total of six FRBs. Accounting for the efficiency of the detection pipeline (90 per cent, see Section 3.4), we estimate the UTMOST FRB discovery rate as ∼63 d per event. This corresponds to a sky rate of 98^{+59}_{-39} events sky^{-1} d^{-1} above a fluence of 8 Jy ms, where the quoted uncertainties represent 1σ Poissonian errors (Gehrels 1986).

Fig. 10 shows UTMOST FRB sky rates (at 843 MHz) with our previous survey (Caleb et al. 2017) (red circle, based on three events) and for this survey (green star, based on six events). Note that, as a result of substantial improvements in our understanding of the flux calibration since the first three FRBs were found, we revise the fluence limit of the Caleb et al. 2017 survey from 11 to 15 Jy ms as the authors overestimated the gain of the telescope. We also show the sky rates at 1.4 GHz measured at Parkes and ASKAP. The Parkes point (blue triangle) lies at 1700 events sky^{-1} d^{-1} down to 2 Jy-ms – derived for the Parkes FRBs after taking fluence incompleteness into

[4] https://github.com/wfarah/pydada

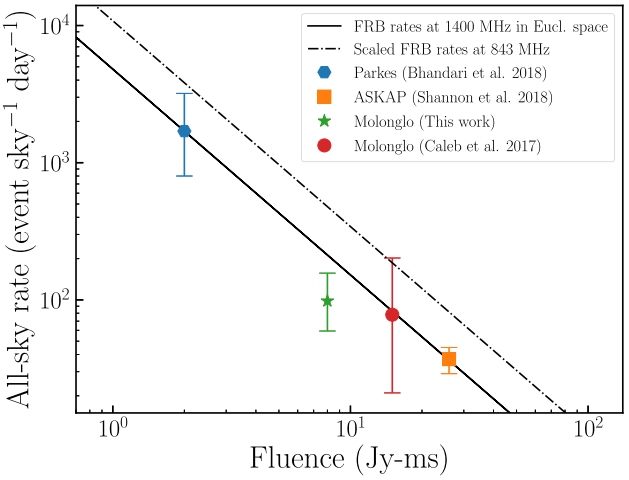

Figure 10. FRB rates in events sky^{-1} d^{-1}, shown as a function of fluence, at Parkes and ASKAP (at 1.4 GHz) and UTMOST (843 MHz). At UTMOST, we show the Caleb et al. (2017) event rate, based on the first three FRBs found (red circle) and the event rate reported here (green star) for six additional FRBs found in a more sensitive survey. The fluence limit was estimated as 11 Jy ms by Caleb et al. (2017): we have revised this to 15 Jy ms, as our understanding of the flux calibration of UTMOST has improved markedly since the first three FRBs were found. The dotted line has a slope of −1.5 in this log–log plane, and represents the expected slope of the cumulative source counts for a Euclidean universe. It is a close match to the event rates seen in *L* band (1.4 GHz) going from ASKAP to Parkes. Assuming a flat spectral index for FRBs, the expected event rate at UTMOST is approximately 215 events sky^{-1} d^{-1} at a sensitivity of 8 Jy ms. We obtain a rate of 98^{+59}_{-39} events sky^{-1} d^{-1} in the present survey, somewhat below the expected rate scaling from the 1.4 GHz rates. We also show (dashed line), the expected event rate at 843 MHz assuming FRBs have a mean spectral index of −1.6 (Macquart et al. 2019). At 8 Jy ms sensitivity, we expect an event rate of ≈480 events sky^{-1} d^{-1}. The event rate at UTMOST falls significantly below this value, indicating that the mean spectral index of FRBs may not be this steep.

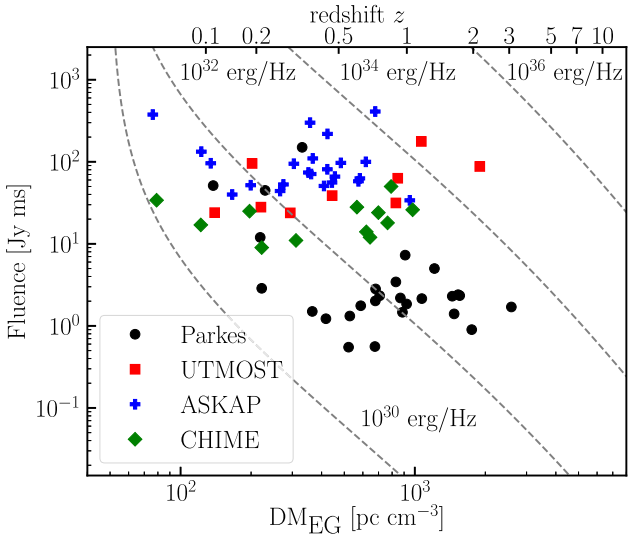

Figure 11. The fluence of FRBs found at Parkes (black), ASKAP (blue), and UTMOST (red) are shown as a function of their extragalactic dispersion measures, DM$_{EG}$, following Shannon et al. (2018). Dashed lines show the fluence evolution with DM for constant spectral energy density sources, due to cosmological effects. The redshift scale corresponding to the DM axis is shown at the top of the plot We assume FRBs have flat spectra and that 83 per cent of baryons are in the IGM which is fully ionized at all z and is composed of 0.75 H and 0.25 He by mass fraction (Zhang et al. 2018).

account (Bhandari et al. 2018). The ASKAP rate is also measured at 1.4 GHz and is 37 events sky^{-1} d^{-1} to a fluence of 26 Jy ms as reported by Shannon et al. (2018). The solid line shows the expected slope of the sky rate as a function of fluence for a Euclidean universe (−1.5 in this log–log plane). It appears to be a close match to the relative event rates going from bright events at ASKAP to weak events at Parkes. Assuming that FRBs have flat spectra, we would expect an event rate at UTMOST, interpolating between Parkes and ASKAP, of approximately 215 events sky^{-1} d^{-1} at a sensitivity of 8 Jy ms. The observed rate however, is 98^{+59}_{-39} events sky^{-1} d^{-1} in the present survey. This observed rate at 843 MHz is therefore approximately 2σ below the expected rate scaling from ASKAP and Parkes for the simple model of Euclidean counts and flat spectrum sources. We also show (dashed line) the expected event rate at 843 MHz assuming FRBs have a mean spectral index of $-1.6^{+0.3}_{-0.2}$ (Macquart et al. 2019). At 8 Jy ms sensitivity, we expect an event rate of ∼480 events sky^{-1} d^{-1}. The UTMOST event rate falls significantly ($\sim 7\sigma$) below this value, arguing against such a steep spectral index.

Given the lower than expected rate at 843 MHz suggests that the spectra of FRBs may turn over at about 1 GHz. This is consistent with a number of recent studies. First, six ASKAP FRBs were observed simultaneously with the Murchison Wide Field array (MWA) but yielded only upper limits on their fluences at 170–200 MHz, indicating that the spectral index of FRBs is no steeper than $\alpha \approx -1$ (Sokolowski et al. 2018). Secondly, and more significantly, the non-detection of FRBs in an 84 d survey made at the Green Bank Telescope (GBT) (Chawla et al. 2017) at 300–400 MHz to a sensitivity of 0.6 Jy ms (for 5 ms events), places an upper limit on the spectral index of FRBs of $\alpha > -0.3$. Ravi & Loeb (2019) discuss these results in detail and propose a number of mechanisms to explain why the spectral energy distribution of FRBs would turn over below ≈1 GHz. The UTMOST results reported here are consistent with these proposals.

In Fig. 11, we show FRB fluences versus extragalactic DM for our sample of nine FRBs (red squares) at 830–850 MHz, 23 ASKAP FRBs (blue crosses) at 1.2–1.6 GHz, 13 CHIME FRBs (green diamonds) at 400–800 MHz, and 19 Parkes FRBs (black circles) at 1.2–1.6 GHz. As has been argued by Shannon et al. (2018), the trend to lower fluence with increasing DM is consistent with FRBs being at cosmological distances (upper scale of plot), based primarily on the ASKAP and Parkes FRBs (as these have all been found at 1.4 GHz). In including our newer UTMOST and the CHIME FRBs on the plot, we have assumed that the FRB spectra are flat, to simplify the comparison of FRBs found in surveys with very different frequency coverage (and note that FRBs might not have flat spectra, as discussed above). Lines of constant energy density are shown for a standard cosmology (see figure caption). Note also that the widely differing frequency channel widths in the surveys affects the DM to which FRBs can be detected, due to the effects of DM smearing (the spectral resolution of UTMOST is 97 kHz, compared to 1 MHz and 336 kHz for ASKAP and Parkes respectively). UTMOST is thus able to probe to higher dispersion measures, and has indeed found two bright, high DM FRBs. It is clear that FRBs span a wide range of intrinsic energies (of order 2 decades) at a given DM, indicating their intrinsic luminosity function is broad.

Table 2. FRB field follow-up campaign with UTMOST. No repeat pulses were found for any FRB. We note that the radio follow-up of FRB181228 took place after the end of this survey, and hence this FRB is not included in this table.

FRB name	Total time (h)	Discovery	Reference[1]
FRB160317	6.3	UTMOST	[1]
FRB160410	2.0	UTMOST	[1]
FRB160608	3.9	UTMOST	[1]
FRB170107	2.0	ASKAP	[2]
FRB170416	5.8	ASKAP	[3]
FRB170428	5.8	ASKAP	[3]
FRB170707	8.2	ASKAP	[3]
FRB170712	10.2	ASKAP	[3]
FRB170827	29.8	UTMOST	[4]
FRB170906	5.1	ASKAP	[3]
FRB170922	10.5	UTMOST	This work
FRB171003	1.9	ASKAP	[3]
FRB171004	2.4	ASKAP	[3]
FRB171019	5.9	ASKAP	[3]
FRB171020	5.8	ASKAP	[3]
FRB171116	3.5	ASKAP	[3]
FRB171213	4.4	ASKAP	[3]
FRB171216	4.2	ASKAP	[3]
FRB180110	4.2	ASKAP	[3]
FRB180119	4.2	ASKAP	[3]
FRB180309	0.5	Parkes	[5]
FRB180528	6.0	UTMOST	This work
FRB181016	2.7	UTMOST	This work
FRB181017	8.1	UTMOST	This work

Note. [1][1] Caleb et al. (2017), [2] Bannister et al. (2017), [3] Shannon et al. (2018), [4] Farah et al. (2018a), [5] Oslowski et al. (2018).

6 FRB FOLLOW-UP

6.1 Radio follow-up

As part of the dynamic scheduling of observations by SMIRF, the fields of our own FRBs and a selection of those found in the ASKAP/CRAFT project were regularly re-observed to search for FRB repetition. The FRB fields searched and the total observing time for each since deployment of the SMIRF scheduler are listed in Table 2. A total of 120 h of follow-up at UTMOST was performed for 23 FRB fields. Typically, observations had a duration of the transit time of the field centre across the FWHP of the primary beam (4°) and, depending on the declination of the FRB, is ∼20 min. No FRBs were seen to repeat during the follow-up programme down to an S/N of 9.

Motivated by the resemblance – in temporal and spectral structure – of FRB181017 to the repeating FRB121102 (Hessels et al. 2019), we conducted a follow-up campaign to search for repeating bursts using more sensitive facilities: the Effelsberg radio telescope and the upgraded Giant Metrewave Radio Telescope (uGMRT).

Effelsberg: Data were obtained on UTC 2018 October 25 and UTC 2018 November 05 using the seven-beam feed array and the high time resolution (54 μs) Pulsar Fast Fourier Transform Spectrometer backend in pulsar search mode (Barr et al. 2013). The data were centred at a frequency of 1.36 GHz with a bandwidth of 300 MHz divided over 512 channels. The receiver was rotated such that three of the seven beams were aligned along the uncertainty arc of the FRB. The localization arc was tiled with 11 partially overlapping pointings (33 beams of 10 arcmin each) along its north–south extend of 2.8°. We searched for pulses in these three beams using HEIMDALL over a range of 30 pc cm^{-3}, centred on the DM of the FRB, and pulse widths in the range 54 μs to 55 ms, down to an S/N of 7. We required that candidate events appear in one beam of the instrument only. This corresponds to a search sensitivity of 0.2 Jy ms for a 1 ms pulse. We found no repeat bursts of the FRB.

uGMRT: Observations of FRB181017 were made on UTC 2018 November 17, 2018 November 27, and 2018 November 29 with the incoherent uGMRT array in band-4 (550–850 MHz). Data were recorded at 327.68 μs with 8192 channels over the band to ensure that the dispersion smearing within a channel is comparable to the time resolution at the DM of the FRB. As the FWHM of the uGMRT beam in this band is ∼37 arcsec, the uncertainty in the FRB declination was tessellated into a strip of 10 individual overlapping pointings at the nominal RA. The data were searched offline using the HEIMDALL single pulse search software for pulses with S/N ≥ 6, DMs in the range 220 pc cm^{-3} ≤ DM ≤ 260 pc cm^{-3} and widths ≤100 ms. Using the radiometer equation, we calculate a theoretical sensitivity of 0.6 Jy at 1 ms for an S/N = 6 detection. RFI mitigation was performed using the CLFD[5] package described in Morello et al. (2019). We did not find any repeat pulses from the FRB in a total of 8.3 h spent on source.

6.2 Optical follow-up

For three of the FRBs reported here (FRB170922 was discovered 2 weeks after data recording, and FRB181016 was discovered during the Australian daytime), a search for possible optical afterglow was conducted using the SkyMapper telescope (Keller et al. 2007). We established an automated system that allows scheduling of an FRB field to be triggered via email. The shortest time from FRB trigger to observations has been ∼2 h but is typically the following night or nights, contingent on weather and field location relative to the Sun and Moon.

FRB181017: no useful science images were produced due to bad weather conditions on site, a 70 per cent illuminated moon and its close proximity (∼15°) to the centre of the FRB localization arc.

FRB180528 and FRB181228: images were taken in the r and i bands for which the photometric depths for a 100 second exposure are $i = 19.17$, $r = 19.54$ (FRB180528) and $i = 20.7$, $r = 21.7$ (FRB181228) at the 95 per cent upper limit (SkyMapper Transient Survey Pipeline, Scalzo et al. 2017).

The follow-up fields were centred on the most likely FRB coordinate as reported in our astronomer's telegrams along with fields to the north and south to cover the 1σ uncertainty in the localization arcs for FRBs detected with the current operation mode at UTMOST (i.e. 4.8°). Observations consist of multiple images centred on the FRB most likely positions, with slight pointing offsets, followed by imaging of the 1σ regions. The localization arc of each FRB was searched for optical transients with reference to existing images from SkyMapper's database, or with reference to images taken on subsequent nights. We found no optical transients that could be associated with our FRB events.

6.3 FRB181228 follow-up

An astronomer's telegram for FRB181228 (Farah et al. 2018d) was issued within 2 h of the event, and there has been considerable follow-up by external parties, attesting to the efficacy of early triggering. No counterparts have been found. An optical transient was found with MASTER PN (Gorbovskoy et al. 2018) in a region

[5]https://github.com/v-morello/clfd

close to the localization arc. This was determined to be a type Ia supernova after spectroscopy was obtained with the Southern African Large Telescope (Buckley et al. 2018). They report the source is likely to be 10 d post-maximum and hosted in the galaxy LEDA 499631, with a redshift in the range 0.025–0.031. The maximum DM inferred redshift of FRB181228 is 0.3. It is thus unlikely that the type Ia supernova is associated with the FRB. X-ray data from Astrosat CZTI was also searched for an associated transient in a 20 s window, with no counterpart found (Anumarlapudi et al. 2019).

7 CONCLUSIONS

We have presented the results of the latest FRB survey conducted with the Molonglo radio telescope, using a newly implemented live machine learning based FRB detection system. We accumulated a total of 344 d on sky searching for FRBs in real-time, discovering six FRBs.

We demonstrated the importance of the real-time detection of FRBs, as evidenced by the discovery of high time and frequency structure in FRB pulse profiles resulting from the capture of the raw data – particularly for our higher S/N events. This has allowed us to probe the properties of some of the narrowest and least scattered FRBs to date. The temporal profile of FRB181017 shows three peaks, with the middle component not centred in time. This argues against a source of underlying periodicity on the $\sim$1 ms time-scales. The FRB dynamic spectrum is similar to our other bright event (FRB170827), as well as to the first repeating FRB (FRB121102), potentially linking repeating and non-repeating FRBs. The frequency structure across the multipeaked profile FRBs argues for an origin associated with the propagation in the host galaxy or the IGM, rather than arising at the source. Moreover, given the triple-peak temporal structure of this FRB, we rule out a lensing scenario by finding no evidence that the voltage data of the leading and trailing peaks are correlated. We encourage the application of this technique to multicomponent FRBs soon to be found with new generation telescopes such as CHIME, MeerKAT, ASKAP, and UTMOST-2D.

We derive an event rate of 98^{+59}_{-39} events sky^{-1} d^{-1} at a fluence limit of 8 Jy ms at 843 MHz. This rate is somewhat below expectation, scaling from the FRB rates found at Parkes and ASKAP, both of which operate at 1.4 GHz, and assuming that the average spectral energy distribution of FRBs is flat. Our results do not agree with the steep negative spectral index estimates for mean FRB spectra of $\approx -1.6 \pm 0.2$ (Macquart et al. 2019), and may indicate that the spectra of FRBs turnover at around 1 GHz, as has been recently suggested by Ravi & Loeb (2019). The CHIME collaboration has reported 13 FRBs in the range 400–800 MHz, and estimate a lower limit on the sky rate of 300 event sky^{-1} d^{-1} to a flux density of 1 (ms/Δt)$^{1/2}$ Jy. Their very high discovery rate should allow the question of a turnover in the spectral energy density of FRBs to be probed in the near future.

We are currently outfitting the NS arm of the telescope for the UTMOST-2D project, which will provide localizations of FRBs from single detections with arcsecond precision. The highly effective machine learning FRB live detection pipeline reported here will be used to trigger full data retention of single pulse events, as a major part of our hunt for FRB hosts.

ACKNOWLEDGEMENTS

We thank Michael Kramer for valuable discussions on FRB scattering tail fitting. We thank Laura Spitler for assistance with the Effelsberg data analysis. The anonymous referee is thanked for comments which clarified our thinking on a number of points. The Molonglo Observatory is owned and operated by the University of Sydney, with support from the School of Physics and the University. The UTMOST project is also supported by the Swinburne University of Technology. We acknowledge the Australian Research Council grants CE110001020 (CAASTRO) and the Laureate Fellowship FL150100148. ATD is supported by an ARC Future Fellowship grant FT150100415. MC and BWS acknowledge funding from the European Research Council (ERC) under the European Union's Horizon 2020 research and innovation programme (grant agreement no. 694745). The national facility capability for SkyMapper has been funded through the Australian Research Council LIEF grant LE130100104, awarded to the University of Sydney, the Australian National University, Swinburne University of Technology, the University of Queensland, the University of Western Australia, the University of Melbourne, Curtin University of Technology, Monash University, and the Australian Astronomical Observatory. SkyMapper is owned and operated by The Australian National University's Research School of Astronomy and Astrophysics. The GMRT is run by the National Centre for Radio Astrophysics of the Tata Institute of Fundamental Research, India. We acknowledge support of GMRT telescope operators for the observations. This research has made use of NASA's Astrophysics Data System.

REFERENCES

Agarwal D., Aggarwal K., Burke-Spolaor S., Lorimer D. R., Garver-Daniels N., 2019, preprint (arXiv:1902.06343)
Anumarlapudi A., Aarthy V., Bhalerao D., Bhattacharya A., Rao A. R., Vadawale S., 2019, Astron. Telegram, 12370
Ashton G. et al., 2019, ApJS, 241, 27
Bailes M. et al., 2017, Publ. Astron. Soc. Aust., 34, e045
Bannister K. W. et al., 2017, ApJ, 841, L12
Barr E. D. et al., 2013, MNRAS, 435, 2234
Barsdell B. R., 2012, PhD thesis, Swinburne Univ. Technology
Bassa C. G. et al., 2017, ApJ, 843, L8
Bhandari S. et al., 2018, MNRAS, 475, 1427
Bhattacharyya S., 2018, JA&A, 39, 47
Breiman L., 2001, Mach. Learn., 45, 5
Buchner J. et al., 2014, A&A, 564, A125
Buckley D. A. H., Gromadzski M., Gorbovskoy E., Lipunov V., Kuhn R., 2018, Astron. Telegram, 12343
Caleb M. et al., 2017, MNRAS, 468, 3746
Caleb M. et al., 2018, MNRAS, 478, 2046
Chatterjee S. et al., 2017, Nature, 541, 58
Chawla P. et al., 2017, ApJ, 844, 140
CHIME/FRB Collaboration, 2019a, Nature, 566, 230
CHIME/FRB Collaboration, 2019b, Nature, 566, 235
Connor L., Lin H.-H., Masui K., Oppermann N., Pen U.-L., Peterson J. B., Roman A., Sievers J., 2016, MNRAS, 460, 1054
Connor L., van Leeuwen J., 2018, AJ, 156, 256
Cordes J. M., Lazio T. J. W., 2002, preprint (astro-ph/0207156)
Cordes J. M., Wasserman I., Hessels J. W. T., Lazio T. J. W., Chatterjee S., Wharton R. S., 2017, ApJ, 842, 35
Deng W., Zhang B., 2014, ApJ, 783, L35
Farah W. et al., 2017, Astron. Telegram, 10867
Farah W. et al., 2018a, MNRAS, 478, 1209
Farah W. et al., 2018b, The Astronomer's Telegram, 11675
Farah W. et al., 2018c, The Astronomer's Telegram, 12124
Farah W. et al., 2018d, The Astronomer's Telegram, 12335
Foster G. et al., 2018, MNRAS, 474, 3847
Gehrels N., 1986, ApJ, 303, 336
Gorbovskoy E. et al., 2018, Astron. Telegram, 12338
Hessels J. W. T. et al., 2019, ApJ, 876, L23
Hogg D. W., 1999, preprint (astro-ph/9905116)

James C. W., Ekers R. D., Macquart J.-P., Bannister K. W., Shannon R. M., 2019, MNRAS, 483, 1342
Jankowski F. et al., 2019, MNRAS, 484, 3691
Keane E. F. et al., 2018, MNRAS, 473, 116
Keller S. C. et al., 2007, Publ. Astron. Soc. Aust., 24, 1
Koay J. Y., Macquart J.-P., 2015, MNRAS, 446, 2370
Law C. J. et al., 2018, ApJS, 236, 8
Lorimer D. R., Bailes M., McLaughlin M. A., Narkevic D. J., Crawford F., 2007, Science, 318, 777
Macquart J.-P., Shannon R. M., Bannister K. W., James C. W., Ekers R. D., Bunton J. D., 2019, ApJ, 872, L19
Main R. et al., 2018, Nature, 557, 522
Marcote B. et al., 2017, ApJ, 834, L8
Masui K. et al., 2015, Nature, 528, 523
McQuinn M., 2014, ApJ, 780, L33
Michilli D. et al., 2018, Nature, 553, 182
Morello V. et al., 2019, MNRAS, 483, 3673
Muñoz J. B., Kovetz E. D., Dai L., Kamionkowski M., 2016, Phys. Rev. Lett., 117, 091301
Muñoz J. B., Loeb A., 2018, Phys. Rev. D, 98, 103518
Oslowski S. et al., 2018, Astron. Telegram, 11385
Osłowski S. et al., 2019, MNRAS, preprint (arXiv:1906.09793)
Palaniswamy D., Li Y., Zhang B., 2018, ApJ, 854, L12
Petroff E. et al., 2016, Publ. Astron. Soc. Aust., 33, e045
Planck Collaboration XIII, 2016, A&A, 594, A13
Ravi V., 2019, MNRAS, 482, 1966
Ravi V., Loeb A., 2019, ApJ, 874, 72
Ravi V. et al., 2016, Science, 354, 1249
Ravi V. et al., 2019, BAAS, 51, 420
Scalzo R. A. et al., 2017, Publ. Astron. Soc. Aust., 34, e030
Shannon R. M. et al., 2018, Nature, 562, 386
Sokolowski M. et al., 2018, ApJ, 867, L12
Stappers B., 2016, Proceedings of MeerKAT Science: On the Pathway to the SKA. Stellenbosch, South Africa
Surnis M. P. et al., 2019, preprint (arXiv:1903.05573)
Tendulkar S. P. et al., 2017, ApJ, 834, L7
van Leeuwen J., 2014, in Wozniak P. R., Graham M. J., Mahabal A. A., Seaman R., eds, The Third Hot-wiring the Transient Universe Workshop. p. 79
Vedantham H. K., Phinney E. S., 2019, MNRAS, 483, 971
Venkatraman Krishnan V. et al., 2019, preprint (arXiv:1905.02415)
Wagstaff K. L. et al., 2016, PASP, 128, 084503
Wayth R. B., Brisken W. F., Deller A. T., Majid W. A., Thompson D. R., Tingay S. J., Wagstaff K. L., 2011, ApJ, 735, 97
Wright E. L., 2006, PASP, 118, 1711
Zhang B., 2018, ApJ, 867, L21
Zhang Y. G., Gajjar V., Foster G., Siemion A., Cordes J., Law C., Wang Y., 2018, ApJ, 866, 149
Zheng Z., Ofek E. O., Kulkarni S. R., Neill J. D., Juric M., 2014, ApJ, 797, 71

This paper has been typeset from a TEX/LATEX file prepared by the author.